

Mathematical and Computer Modelling of Dynamical Systems

Methods, Tools and Applications in Engineering and Related Sciences

ISSN: (Print) (Online) Journal homepage: <https://www.tandfonline.com/loi/nmcm20>

Mathematical Modelling of Non-Linear Transient Long Waves by using Finite Element Method in an Irregular Shaped Harbour

Sukhwinder Kaur, Prashant Kumar & Rajni

To cite this article: Sukhwinder Kaur, Prashant Kumar & Rajni (2021) Mathematical Modelling of Non-Linear Transient Long Waves by using Finite Element Method in an Irregular Shaped Harbour, *Mathematical and Computer Modelling of Dynamical Systems*, 27:1, 411-428, DOI: [10.1080/13873954.2021.1973510](https://doi.org/10.1080/13873954.2021.1973510)

To link to this article: <https://doi.org/10.1080/13873954.2021.1973510>



© 2021 The Author(s). Published by Informa UK Limited, trading as Taylor & Francis Group.



Published online: 07 Sep 2021.



Submit your article to this journal [↗](#)



Article views: 204



View related articles [↗](#)



View Crossmark data [↗](#)

Mathematical Modelling of Non-Linear Transient Long Waves by using Finite Element Method in an Irregular Shaped Harbour

Sukhwinder Kaur^a, Prashant Kumar^a  and Rajni^b

^aDepartment of Applied Sciences (Mathematics), National Institute of Technology, Delhi, India; ^bJindal Global Business School, O. P. Jindal Global University, Sonapat, Haryana, India

ABSTRACT

Extreme waves significantly affect the coastal structures, activities, and population. Therefore, investigation of extreme wave impact on coastal regions is essential. In this study, a mathematical model is presented to analyse the impact of transient long waves on coastal structures. The mathematical model is constructed based on the Boussinesq equation (BE) with variable water depth including dispersion properties. The numerical solution of BE is constructed by using FEM. The present numerical model is validated through the existing study of Lepelletier (1981) and convergence analysis is also conducted to determine the convergence rate. The present FEM model is implemented on realistic Paradip port, Odisha, India to determine the wave amplitude at various record stations. In addition, the impact of incident waves with angular variation is analysed in the Paradip port. The causes and countermeasures have been proposed based on the simulation results to improve the resonance in the port.

ARTICLE HISTORY

Received 9 April 2020
Accepted 20 August 2021

KEYWORDS

Boussinesq equation; transient long waves; finite element method; paradip port

1. Introduction

The non-linear transient long waves propagating towards the coastal region from various directions induce harbour resonance as they interact with the coastal boundaries of the harbour wall. This resonance aggravates/perturbed wave motion inside the harbour due to the impact of diffraction, reflection, and refraction of waves with the coastal boundaries and causes severe damage to the coastal boundaries, structures, moored ship, mooring ropes, and fender in the harbour. Although it is hard to measure the long waves and their effect on the coastal region, as they propagate in the ocean, their wave amplitude is small and wave period is large (i.e., $10 \sim 10^2$ minutes), but they build up their amplitude when approaching the coastal region. Thus, it is imperative to develop an efficient and reliable numerical model for studying the impact of long waves in the time domain.

To have a better comprehension of wave effects in the coastal region, enormous work has been carried out in the past decades to develop both linear and non-linear models. Linear models usually rely on the Helmholtz equation [1–3] or Mild Slope equation [4–6] whilst the

CONTACT Prashant Kumar  prashantkumar@nitdelhi.ac.in  Department of Applied Sciences (Mathematics), National Institute of Technology, Delhi 110040, India

© 2021 The Author(s). Published by Informa UK Limited, trading as Taylor & Francis Group.
This is an Open Access article distributed under the terms of the Creative Commons Attribution-NonCommercial License (<http://creativecommons.org/licenses/by-nc/4.0/>), which permits unrestricted non-commercial use, distribution, and reproduction in any medium, provided the original work is properly cited.

non-linear models on the Boussinesq equation (BE) [7–9]. The depth-averaged Boussinesq model of variable bathymetry was first introduced by Peregrine [10] to determine the non-linear transformation of multi-directional surface waves in shallow water. Several researchers developed the numerical model based on the Peregrine [10] equation to examine the wavefield inside the harbour due to non-linear transient long waves. Initially, BE was solved by the finite difference method (FDM) using a rectangular grid [11,12]. However, if the wave field is computed inside a 2-dimensional (2-D) domain with complex geometry by using a uniform finite-difference grid, there may be a loss of computational accuracy.

To overcome this problem, researchers emphasize more on unstructured FEM for approximating the BEs. Firstly, many FEM models were constructed for conventional Boussinesq equations (CBEs) [13,14]. Recently, FEM has been applied to Modified Boussinesq equations (MBE) [15–17]. Woo and Liu [18] developed a new FEM technique depending on Petrov–Galerkin weighted residual method, with cubic B-splines as the weighting function for one-dimensional, fully non-linear, and weakly dispersive wave propagation without using auxiliary variables. This method is difficult to apply to the complex geometry in the 2-D domain as the cubic spline functions cannot be easily extended to the 2-D irregular/unstructured grid system. Lepelletier [7] proposed a finite element model using Wu's equations [19] to examine the excitation of the harbour by non-linear transient long waves.

Recently, models have been constructed to study the wave-induced oscillations caused by incoming long or short waves propagating from the open sea towards the realistic harbours using different numerical techniques. For example, a mathematical model based on the boundary element method (BEM) is applied to estimate the wave response inside the Pohang New Harbour in South Korea [20] and Paradip port in India [21–23]. FEM and Hybrid FEM are utilized to analyse the wave response inside the Marina di Carrara harbour in Italy [24] and the Pohang New Harbour in South Korea [25], respectively. Higher-order FEM is used to analyse the propagation of waves excited by internal elements [26]. Such studies were predominantly concerned with linear models. However, excitation of realistic harbour due to non-linear transient long waves remains limited except for a few studies such as FEM is applied to investigate the wave response inside the Hilo Bay, Hawaii [27].

In this study, a sensitivity analysis based on the direction of the incident waves has been performed to estimate/determine the influence of resonant waves in the realistic harbour. The BE is used to investigate the transient long waves response on the irregular-shaped harbour. The BE is solved in the domain of interest (bounded region of the port) by using FEM with non-uniform mesh elements. The effects of dispersion properties including the variable bathymetry are incorporated in the present numerical model. The current numerical scheme is validated with the existing studies of Lee (1971) [28] and Ippen and Goda (1963) [29], and Lepelletier (1981) [7]. Further, the convergence analysis is also carried out for the rectangular domain to determine the order of convergence. Based on the validation, the present numerical model is implemented on the realistic port such as Paradip port, Odisha, India to determine the wave amplitude at various key locations. The angular variation of the incident waves inside the Paradip port is also determined to understand the possible influence of different directional waves. In

addition, the wave amplitude in the interior of Paradip port under the different resonance modes is also estimated for directional incident waves to identify the safe location for moored vessels.

The paper is arranged as follows. Section 2 describes the mathematical formulation of the BE obtained using FEM. The validation of the present numerical model with the existing study along with convergence analysis is provided in section 3. The implementation of the current numerical model on the complex geometry such as Paradip port is given in section 4. Section 5 contains the discussion and conclusion.

2. Mathematical Formulation

2.1. Governing Equations

In order to investigate the long wave-induced oscillation in a harbour, the Cartesian coordinate system O - xyz is located at the harbour entrance with the y -axis being taken along the shoreline, the x -axis is directed towards the open sea, and the z -axis vertically upward. For simplicity, it is assumed that the fluid is inviscid, incompressible, and fluid flow is irrotational. The governing equations (i.e., the continuity and momentum equations) for long waves after using the dimensionless variable and boundary conditions are expressed as

$$\frac{\partial \eta}{\partial t} + [d \phi] = \mu \left[\left\{ \frac{d}{2} (d \phi) - \frac{d^2}{3} {}^2\phi \right\} d \right] + O(\mu^2) \quad (2.1)$$

$$\frac{\partial \phi}{\partial t} + \eta - \mu \frac{\partial}{\partial t} \left[\frac{d}{2} (d \phi) - \frac{d^2}{6} {}^2\phi \right] = O(\mu^2) \quad (2.2)$$

where, $\phi = \phi(x, y, t)$ represents the velocity potential function, $\eta = \eta(x, y, t)$ is the wave elevation, $d = d(x, y)$ is the variable water depth, $\mu = (d_0/\lambda)^2$ is the dispersive parameter, where λ is the wavelength, d_0 is the constant water depth. Further, on combining equations (2.1) and (2.2), we get.

$$\phi_{tt} - (d \phi) - \mu \left[\frac{d}{2} (d \phi_{tt}) - \frac{d^2}{6} {}^2\phi_{tt} \right] + \mu \left[\left(\frac{d}{2} (d \phi) - \frac{d^2}{3} {}^2\phi \right) d \right] = O(\mu^2) \quad (2.3)$$

2.2. Model geometry

The domain of interest is divided into two regions as bounded region (Ω_1 or harbour region) and unbounded region (Ω_2 or open sea region) (see Figure 1). It is assumed that the scattering and energy dissipation are contained within the region L with partially reflective boundary ∂L . The bounded region Ω_1 with variable water depth d is enclosed by the partially reflecting solid boundary ∂L and pseudo boundary $\partial\Omega_1$ and unbounded region Ω_2 with constant water depth d_0 is the open sea region with boundary $\partial\Omega_2$ lying at some finite distance (see Figure 1). In bounded region Ω_1 , the velocity potential function ϕ_1 satisfies the BE Eq. (2.3).

In unbounded region Ω_2 , the dispersion effect is negligible, and Eq. (2.3) is given by

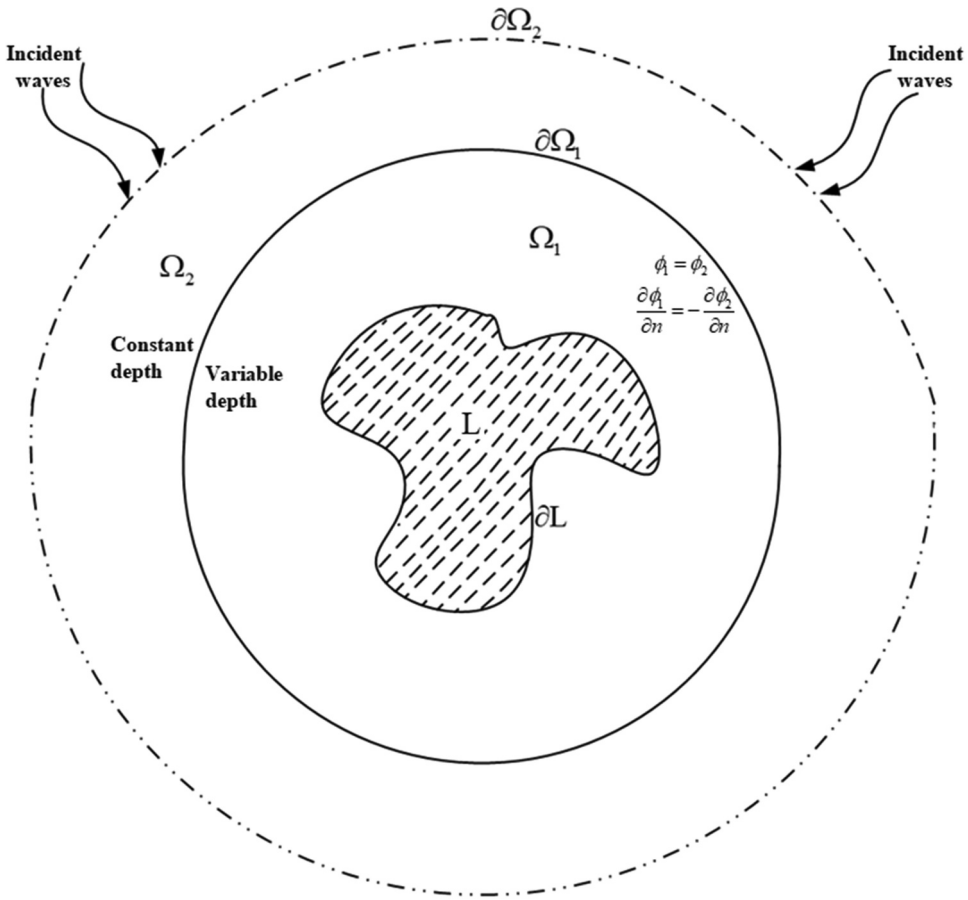


Figure 1. Model geometry with the bounded region and open sea region.

$$\phi_{2,tt} - \nabla^2 \phi_2 = 0 \tag{2.4}$$

The velocity potential function ϕ_2 is expressed as

$$\phi_2 = \phi_I + \phi_R + \phi_S \tag{2.5}$$

where $\phi_I, \phi_R,$ and ϕ_S represents the incident, reflective, and radiated wave potential functions, respectively. In the Ω_2 region, radiated waves propagate towards the open sea, and the solution of the radiated wave potential is obtained by using the Sommerfield radiation boundary condition in the time domain along the boundary $\partial\Omega_2$, is expressed as

$$\phi_S = \text{Re} \sum_{n=0}^{n=\infty} \phi_{S,n}(k) H_n^1(kR) e^{-i\omega t} \cos(n\alpha) dk \tag{2.6}$$

where H_n^1 denotes the Hankel function of the first kind and n^{th} order, α is the angular variation lie between 0 to π , and $\phi_{s,n}(k)$ is the function of k that depends on the geometry of the radiative disturbance. The Sommerfeld radiation boundary condition in the time domain along the boundary $\partial\Omega_2$ is written as

$$\lim_{R \rightarrow \infty} \left[\frac{\partial \phi_s}{\partial n} + \phi_{s,t} + \frac{1}{2R} \phi_s \right] = 0 \tag{2.7}$$

For a semi-infinite domain with straight and perfectly reflective coastline, parallel to the y-axis

$$\frac{\partial \phi}{\partial n} = 0 \text{ along } \alpha = \frac{\pi}{2}, \frac{3\pi}{2} \tag{2.8}$$

The sinusoidal wave is taken as the incident-reflective wave system and is expressed as follows

$$\phi_I + \phi_R = \sum_{N=0}^{N=\infty} A_n \sin[n(\omega t - kx - \beta)] + \sum_{N=0}^{N=\infty} A_n \sin[n(\omega t + kx - \beta)] \tag{2.9}$$

where β represents the incident wave angle and ω is the angular frequency which is related to the wave number k through the dispersion relation $\omega^2 = gk \tanh(kd_0)$, where g is the acceleration due to gravity. Finally, a matching boundary condition on the boundary $\partial\Omega_1$ is applied to connect the bounded and the unbounded region, which is done by equating the equation of continuity of flow rate and wave elevation across the boundary $\partial\Omega_1$, and is expressed as

$$\phi_1 = \phi_2 \text{ along } \partial\Omega_1 \tag{2.10}$$

$$\frac{\partial \phi_1}{\partial n} = - \frac{\partial \phi_2}{\partial n} \text{ along } \partial\Omega_1 \tag{2.11}$$

In FEM formulation, firstly the weak formulation over the computational domain as shown in [Figure 1](#) is expressed as

$$\begin{aligned} & \iint_{\Omega_1} [\phi_{1,t} \tilde{\phi}_1 + h \phi_1 \cdot \tilde{\phi}_1] d\Omega + \iint_{\Omega_2} \phi_{2,t} \tilde{\phi}_2 d\Omega \\ & + \iint_{\Omega_2} \phi_2 \cdot \tilde{\phi}_2 d\Omega + \mu \iint_{\Omega_1} \left[\frac{h^2}{3} \phi_{1,t} \cdot \tilde{\phi}_1 + \frac{h}{6} \tilde{\phi}_1 \phi_{1,t} \cdot h \right] d\Omega \\ & - \mu \iint_{\Omega_1} \left[\frac{h}{6} \phi_{1,t} \tilde{\phi}_1 \cdot h + \frac{h}{3} (h \cdot \phi_1) (h \cdot \tilde{\phi}_1) \right] d\Omega \\ & - \int_{\partial\Omega_2} \left[\tilde{\phi}_2 \frac{\partial \phi_2}{\partial n} \right] d(\partial\Omega) = \int_{\partial\Omega_1} \left[\tilde{\phi}_1 \frac{\partial \phi_1}{\partial n} \right] d(\partial\Omega) \end{aligned} \tag{2.12}$$

with initial condition

$$\iint_{\Omega_i} \phi_i \tilde{\phi}_i d\Omega = \iint_{\Omega_i} \phi_{i,t} \tilde{\phi}_i d\Omega = 0 \text{ at } t = 0, i = 1, 2 \tag{2.13}$$

On solving integrals presented in Eq.(2.9) using FEM, the computational domain Ω_1 is subdivided into non - overlapping linear triangular elements, and the functions ϕ_i and $\tilde{\phi}_i, i = 1, 2$ are expressed in terms of basis function H_i and the unknown nodal value $\phi_{i,j}^e$ and $\tilde{\phi}_{i,j}^e, i = 1, 2$ at $j = 1, 2, 3$ as

$$\phi_i^e = \sum_{j=1}^3 H_j(x, y) \phi_{i,j}^e(t) \tilde{\phi}_i^e = \sum_{j=1}^3 H_j(x, y) \tilde{\phi}_{i,j}^e(t) \tag{2.14}$$

The linear triangular shape functions are given as follows

$$H_j = \frac{d_j + e_j x + f_j y}{2A_e} \tag{2.15}$$

where $d_i = x_j y_k - y_j x_k, e_i = y_j - y_k, f_i = x_k - x_j, i, j, k,$ permutes in natural order and A_e denotes the area of the triangular element. The weak formulation is converted into matrix formulation and expressed as follows

$$\tilde{\phi}^T \{M_1 \phi_{tt} + M_2 \phi_t + M_3 \phi = F(t)\} \tag{2.16}$$

with initial conditions

$$\tilde{\phi}^T N \phi(0) = \tilde{\phi}^T N \phi_t(0) = 0 \tag{2.17}$$

where $\phi = [\phi_1 \phi_2]^T, M_1, M_2,$ and M_3 are the positive symmetric matrices, and $F(t)$ is the known vector consisting of an incident - reflected wave system. Since the Eqs. (2.16) and (2.17) holds for all vectors $\tilde{\phi}$. So, the corresponding coefficients to vector $\tilde{\phi}$ vanishes and Eqs. (2.16) and (2.17) becomes

$$M_1 \phi_{tt} + M_2 \phi_t + M_3 \phi = F(t) \tag{2.18}$$

With initial conditions

$$N \phi(0) = N \phi_t(0) = 0 \tag{2.19}$$

Finally, the above obtained second order non-linear system is solved by using the implicit - explicit method. The Eq. (2.18) is discretized in the time domain using an implicit - explicit technique as follows [30]:

$$M_1 a_{n+1}^{i+1} + M_2 v_{n+1}^{i+1} + M_3 d_{n+1}^{i+1} = F(t_{n+1}) \tag{2.20}$$

where

$$\left. \begin{aligned} d_{n+1}^{i+1} &= \tilde{d}_{n+1} + \Delta t^2 \beta a_{n+1}^{i+1} \\ v_{n+1}^{i+1} &= \tilde{v}_{n+1} + \Delta t \gamma a_{n+1}^{i+1} \\ \tilde{d}_{n+1} &= \tilde{d}_n + \Delta t \tilde{v}_n + \frac{\Delta t^2}{2} (1 - 2\beta) a_n \\ \tilde{v}_{n+1} &= \tilde{v}_n + \Delta t (1 - \gamma) a_n \end{aligned} \right\} \tag{2.21}$$

where, Δt represents the time step, β and γ represents the numerical parameters that govern the stability and accuracy of the linear scheme, and $d_{n+1}, v_{n+1},$ and a_{n+1} are the discretized values at t_{n+1} of $\Phi, \Phi_v,$ and $\Phi_{tt},$ respectively. Substituting Eq. (2.21) in Eq. (2.20) yields

$$M^i v_{n+1}^{i+1} = G_{n+1} \quad (2.22)$$

where

$$\left. \begin{aligned} M^i &= \frac{1}{\gamma \Delta t} M_1 + M_2 + \frac{\beta \Delta t}{\gamma} M_3 \\ G_{n+1} &= F(t_{n+1}) + \frac{M_1}{\Delta t \gamma} \tilde{v}_{n+1} - M_3 \left(\tilde{d}_{n+1} - \frac{\Delta t \beta}{\gamma} \tilde{v}_{n+1} \right) \end{aligned} \right\} \quad (2.23)$$

Lastly, the wave elevation $\eta(x, y, t)$ is derived from $\phi(x, y, t)$ as follows

$$\eta = -\phi_t + O(\mu) \quad (2.24)$$

3. Numerical Validation and Convergence

3.1 Validation of the current numerical technique

To validate the present numerical scheme on the rectangular domain, the rectangular domain is discretized using the non-uniform triangular mesh elements. A different finite element mesh configuration for each harbour length is required and consequently, only a few numerical runs were performed for comparison with the existing studies in the literature. The finite element mesh configuration for rectangular domain using unstructured triangular element where the coordinates are normalized with respect to wavelength (λ) is shown in Figure 2. The wave amplification factor is computed at the back wall of the rectangular domain corresponding to the non-dimensional wave number kl , where l represents the length of the rectangular

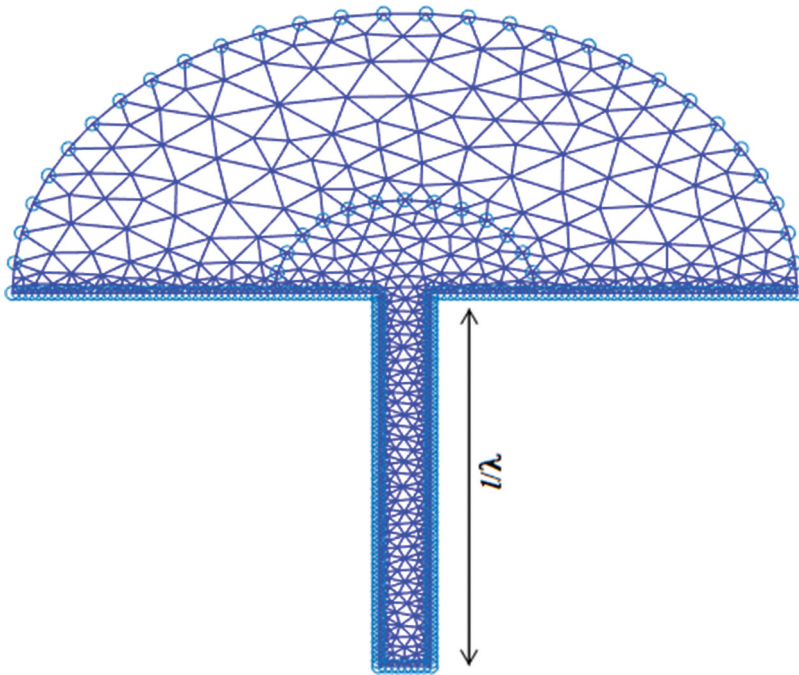


Figure 2. The rectangular domain with non-uniform FEM mesh discretization.

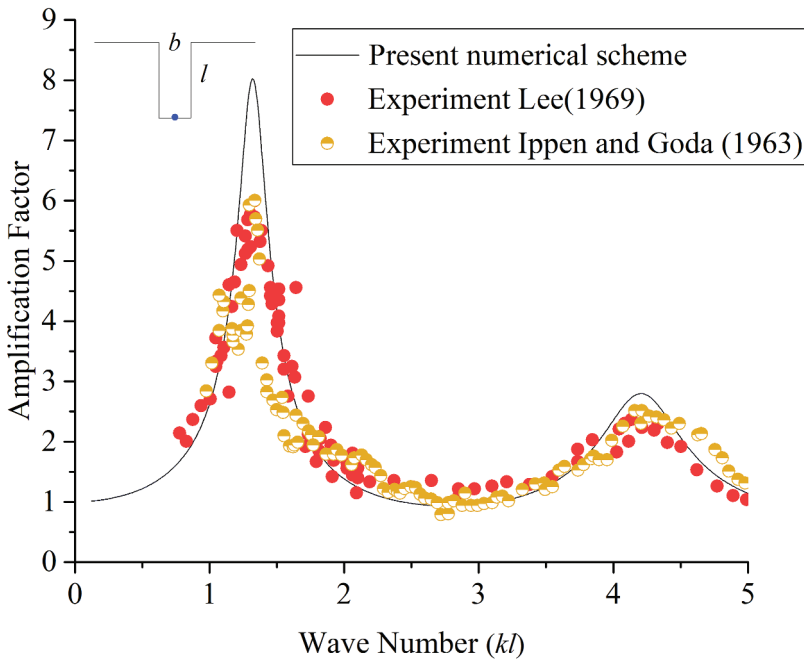


Figure 3. Comparison of the amplification factor at the centre of the back wall of the rectangular harbour corresponding to the dimensionless wave number (kl) for the present numerical scheme, Ippen and Goda (1963), and Lee (1971) study.

domain and is presented in Figure 3. The experimental data of Ippen and Goda (1963) [28] and Lee (1971) [29] study is collected at the centre of the back wall of the rectangular harbour and a good agreement between the present numerical results and existing experimental studies of Lee (1971) [28] and Ippen and Goda (1963) [29] is obtained. The results reveal that the first resonant mode occurs at $kl = 1.32$ and the second at $kl = 4.2$. Further, corresponding to the high amplification (i.e., corresponding to peak value), the wave elevation (η) profile is analysed for the rectangular domain, and results are validated with simulations of Lepelletier [7].

To compute the wave elevation (η) profile near the first and second resonant mode (i.e., around $kl = 1.32$ and $kl = 4.2$), the computational domains are discretized into 1529 and 2289 triangular elements using unstructured triangular mesh, respectively. The normalized configuration of the rectangular harbour around the first and second resonant mode with depth 10 cm and 6 cm and harbour length 41 cm and 53 cm is presented in Figure 4a and 4c, respectively. Figure 4 compares the results of the present numerical scheme (blue) with Lepelletier [7] (pink) at the back wall (W) (see Figure 4) of the fully open rectangular harbour. The present numerical scheme results are obtained by using the Finite Element Method (FEM) and the results reveal good agreement with the previous well-defined study of Lepelletier [7]. Therefore, the present FEM model is validated and implemented on any complex domain or realistic harbour.

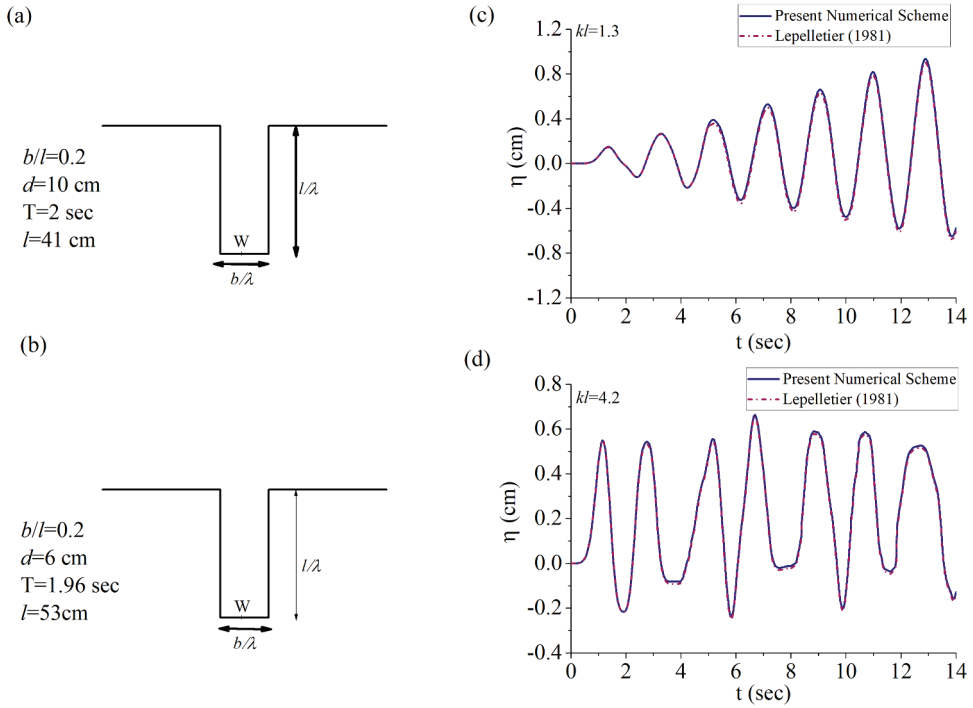


Figure 4. The normalized configuration of the rectangular harbour corresponding to the (a) first and (c) second resonant mode is presented in the left panel of the figure and a comparison of the current numerical scheme (blue) with the Lepelletier [7] results (pink) around the (b) first and (d) second resonant mode at the back wall (W) is shown in the right panel of the figure.

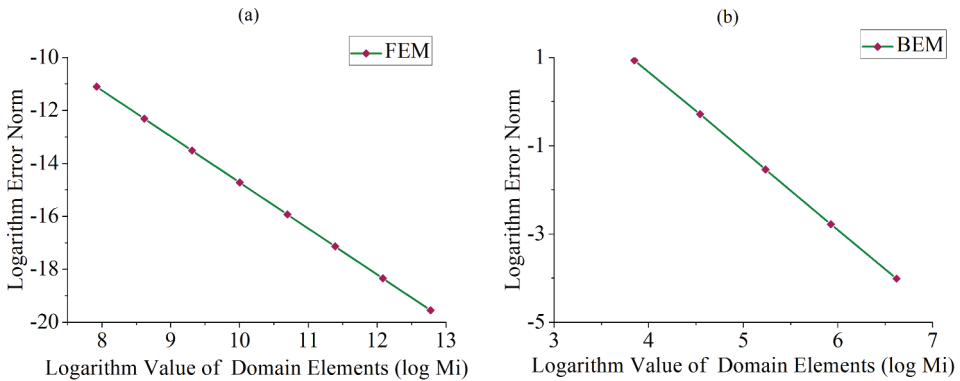


Figure 5. The comparison of the logarithmic error norm with respect to the logarithmic value of segment division ($\log M_i$) for the present numerical FEM scheme (a), and BEM (b).

3.2 Convergence analysis

The convergence analysis is carried out to determine the numerical accuracy of the present numerical scheme. The convergence analysis is performed separately on the rectangular domain for the current numerical technique and the BEM. For this, the rectangular domain is discretized into $M_1 = 2000$, $M_2 = 4000$, and $M_3 = 6000$ discrete triangular elements. The order of convergence (a) is obtained from the following relation

$$a = \frac{\log(Er_1/Er_2)}{\log(M_2/M_1)} \quad (3.1)$$

where $Er_1 = \phi^{M_1} - \phi^{M_3}$ and $Er_2 = \phi^{M_2} - \phi^{M_3}$. The logarithmic error norm and the error norm are presented in Figure 5, and it is found in both BEM and FEM that as the number of segments increases, the error norm eventually decreases. This indicates that both numerical techniques are stable, whereas the current numerical technique demonstrates a better numerical accuracy as compared to the BEM. The order of convergence of the current numerical technique is 1.74 while 1.56 for BEM.

4. Simulation Results

4.1 Implementation on Paradip port

Paradip Port ($20^{\circ}-15'-55.14''N$ and $20^{\circ}-14'-27.34''E$), situated in the Jagatsinghpur district of Odisha, India, is the largest commercial port for coastal trade. Thus, it plays a vital role in the economic growth of India. The topographic view of the Paradip port is shown in Figure 6 and

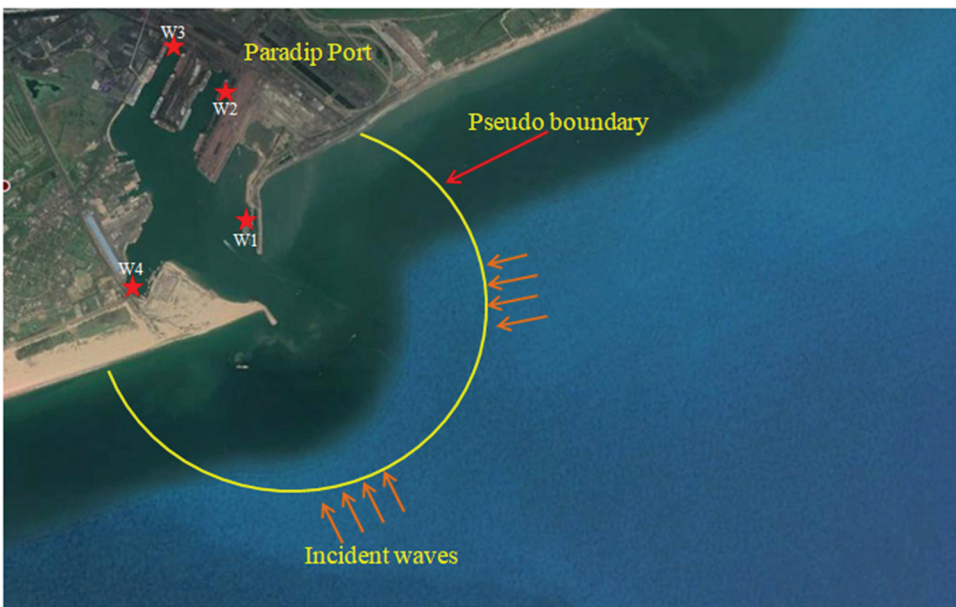


Figure 6. Bird view image of the Paradip port, Odisha, along with four record stations (W1 to W4) marked at the different key locations inside the port. The orange arrows represent the incident waves propagating towards the port's entrance.

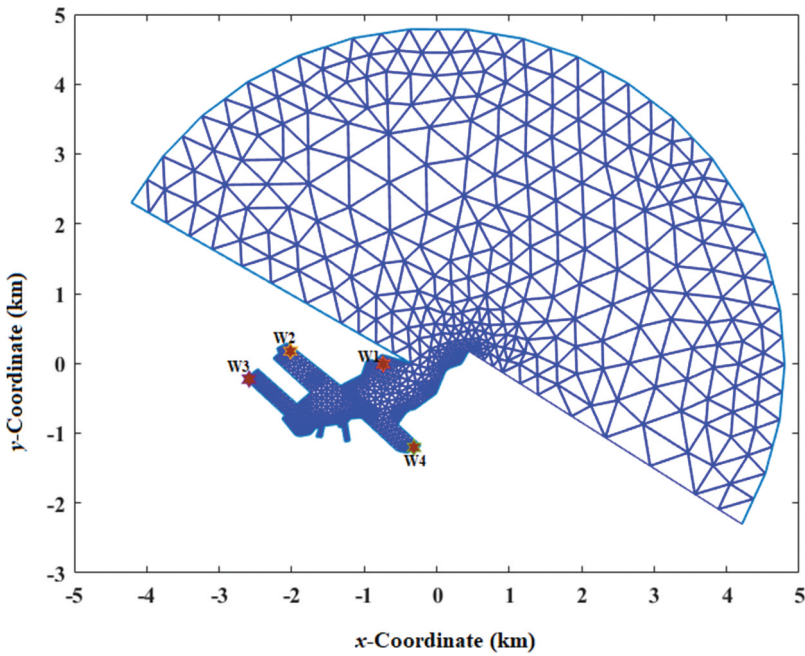


Figure 7. The discretized image of the Paradip port using the non-uniform triangular mesh elements with semi-circular pseudo boundary centred at the entrance. Four record stations from W1 to W6 are placed at the various key locations in the Paradip port.

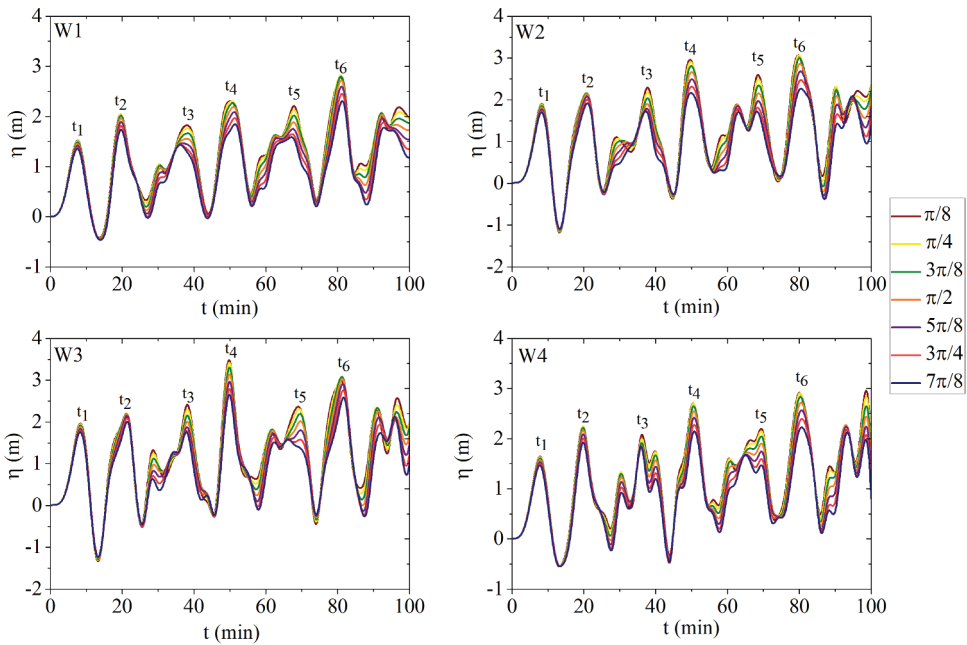


Figure 8. Wave elevation (m) profile corresponding to time (min) at four key locations W1 to W4 inside the Paradip Port for seven different incident wave angles from $\pi/8$ to $7\pi/8$.

the yellow semi-circular arc is the pseudo boundary at a distance of 4.8 km from the entrance and represents the interface between the unbounded (open sea) and bounded (harbour) region. Paradip port has experienced extreme waves oscillation due to seasonal variations [31] and consequently affects numerous activities/operations such as product loading and unloading, port boundary breakage, etc. Therefore, a better understanding of the ocean waves arriving towards the port at different incident angles is essential for the protection of moored vessels. The four record stations are selected inside the Paradip port and labelled as W1 to W4 to determine the wave amplitude at different angular variations. The Paradip Port is discretized into 4001 discrete irregular triangular mesh elements to perform the numerical simulation (see Figure 7).

4.1.1. Wave elevation profile for the Paradip port

The present numerical technique is used to investigate the variations in wave elevation due to incident waves reaching/striking the port at different angles. For this, seven different incident wave angles $\beta = \pi/8, \pi/4, 3\pi/8, \pi/2, 5\pi/8, 6\pi/8,$ and $7\pi/8$ are considered at selected key locations (W1 to W4) inside the Paradip port. In Figure 8, the wave elevation profile is shown at four record stations W1 to W4 of the Paradip port corresponding to time (min) with angular variation $\beta = \pi/8, \pi/4, 3\pi/8, \pi/2, 5\pi/8, 6\pi/8,$ and $7\pi/8$. It is evident that for all directional incident waves, the peak or maximum wave amplitude is obtained at the period $t_1 = 7.6$ min, $t_2 = 19.6$ min, $t_3 = 38$ min, $t_4 = 50.1$ min, $t_5 = 67.8$ min, and $t_6 = 80.8$ min, respectively, and the wave amplitude varies with the change in the direction of the incident wave over the four selected key locations.

The surface wave elevation (η) corresponding to the first peak period (i.e., $t_1 = 7.6$) is higher at record stations W2 and W3 as compared to W1 and W4. For the second peak period (i.e., $t_2 = 19.6$), the strong amplitude is generated near the record station W4. At the third (i.e., $t_3 = 38$) and fifth (i.e., $t_5 = 67.8$) peak period, the largest wave height is obtained around the W3 and W2 record stations, respectively. However, the maximum wave height is seen at the fourth (i.e., $t_4 = 50.1$) and sixth (i.e., $t_6 = 80.8$) peak period compared to other peak periods over all four record stations, yet strongest near the record station W3. Further, the incident wave with wave angle $\beta = \pi/8$ produces strong oscillations in the port and lower for wave angle $\beta = 7\pi/8$ at all the four key locations. Therefore, an incident wave arriving towards the port's entrance from various directions at different peak periods generates strong elevation at different key locations inside the Paradip port. In addition, the surface wave amplitude is determined in the interior of the port with respect to different wave periods and wave direction in the next subsection.

4.1.2. Ocean surface wave height

As a significant increase in wave height is evident at the peak periods $t_1 = 7.6$ min, $t_2 = 19.6$ min, $t_3 = 38$ min, $t_4 = 50.1$ min, $t_5 = 67.8$ min, and $t_6 = 80.8$ min, respectively, for all incoming waves with different incident angles over the four selected key locations in Paradip port. To get a deeper insight into the interrelation between the wave height (η), peak period and incident wave angle, the wave height contour plots corresponding to the first four peak periods at incident wave angles $\beta = \pi/8, \pi/4, 3\pi/8, \pi/2, 5\pi/8, 6\pi/8,$ and $7\pi/8$ are estimated in Paradip Port and displayed in Figures 9–12. For the first peak wave period

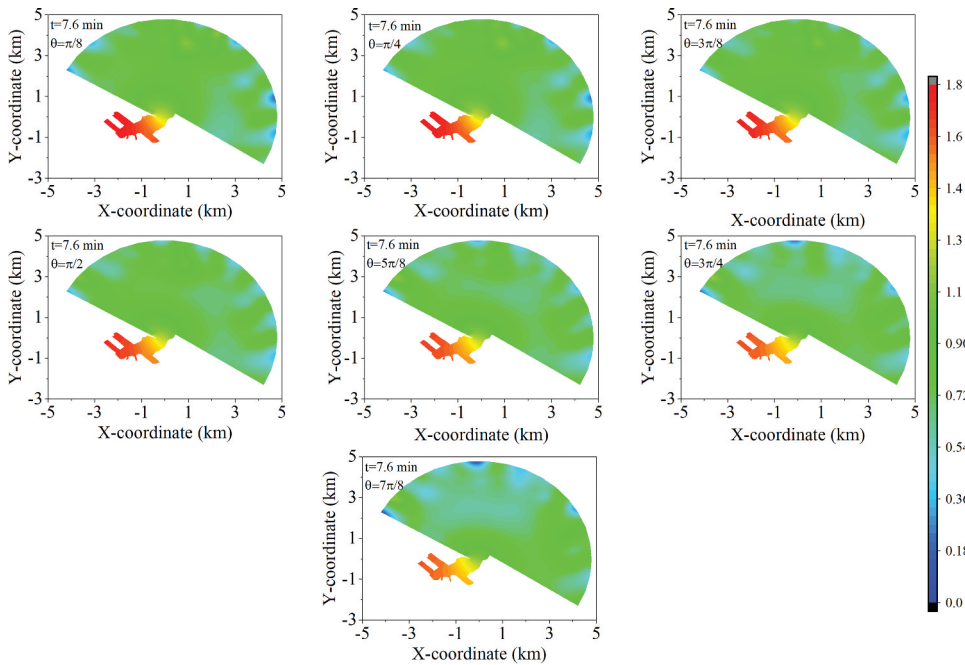


Figure 9. Wave height contour plots corresponding to the first peak period (i.e., $t_1 = 7.6$ min) for the directional incident wave angle with from $\pi/8$ to $7\pi/8$.

(i.e., $t_1 = 7.6$ min), the strongest waves are observed near the region enclosing the record stations W2 and W3 at all directional incident wave angles, which further decreases near the record stations W1 and W4 including the port's entrance (see Figure 9).

In addition, the wave elevation at incident wave angles $\beta = \pi/8, \pi/4,$ and $3\pi/8$ has higher amplification in the interior of the Paradip port as compared to other directional incident waves. While the counter-responses are evident at the second peak period (i.e., $t_2 = 19.6$ min) (i.e., wave height increases near the region enclosing record stations W1 and W4 and decreases near the record stations W2 and W3) (see Fig. 9 and 10). Further, the incident wave angles $\beta = \pi/8, \pi/4,$ and $3\pi/8$ produce strong oscillations inside the Paradip port. The wave height is significantly reduced at wave angle $\beta = 7\pi/8$ compared to other directional incident wave angles (see Fig. 9 and 10). It means that incident waves at angles $\beta = 6\pi/8$ and $7\pi/8$ are the safest for the second wave period inside the Paradip port for loading and unloading.

As the peak wave period increases from 19.6 min to 38 or 50.1 min, the significant variations in wave elevation are evident in the Paradip port. The strongest wave height lies between 1.7 and 2.4 m is seen inside the port at $t_3 = 38$ min compared to the peak period $t_1 = 7.6$ min and $t_2 = 19.6$ min (see Figure 11). This suggests that the incident wave with a large wave period generates a strong wave oscillation inside the port. Further, the strongest waves are estimated at incident wave angles $\beta = \pi/8$ and $\pi/4$ at the record stations W3 and W2, and the safest location is identified near W1 and W4 at incident wave angles $\beta = 6\pi/8$ and $7\pi/8$.

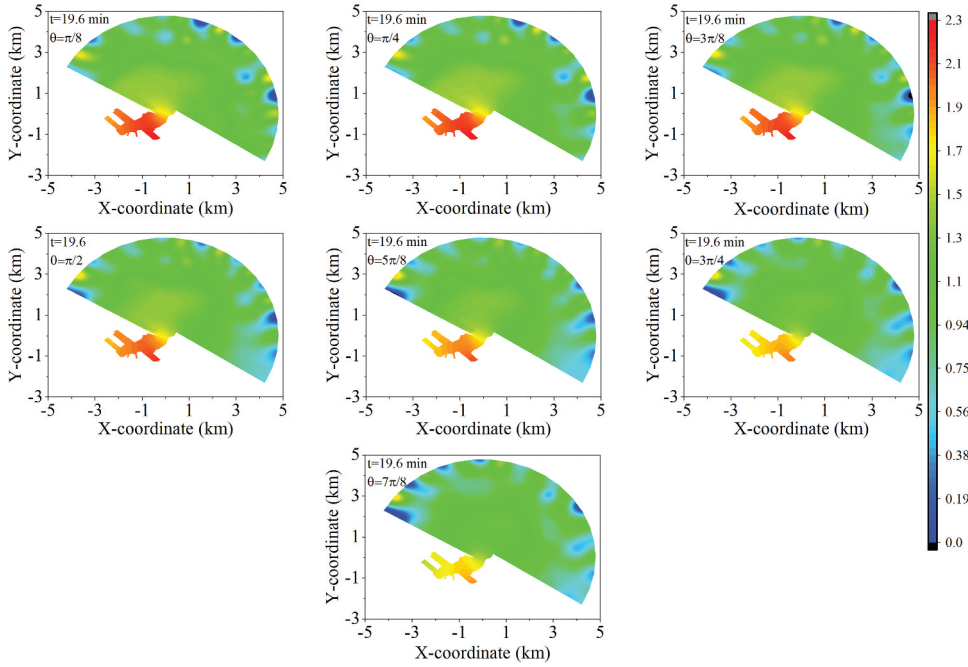


Figure 10. Wave height contour plots corresponding to the second peak period (i.e., $t_2 = 19.6$ min) for the directional incident wave angle from $\pi/8$ to $7\pi/8$.

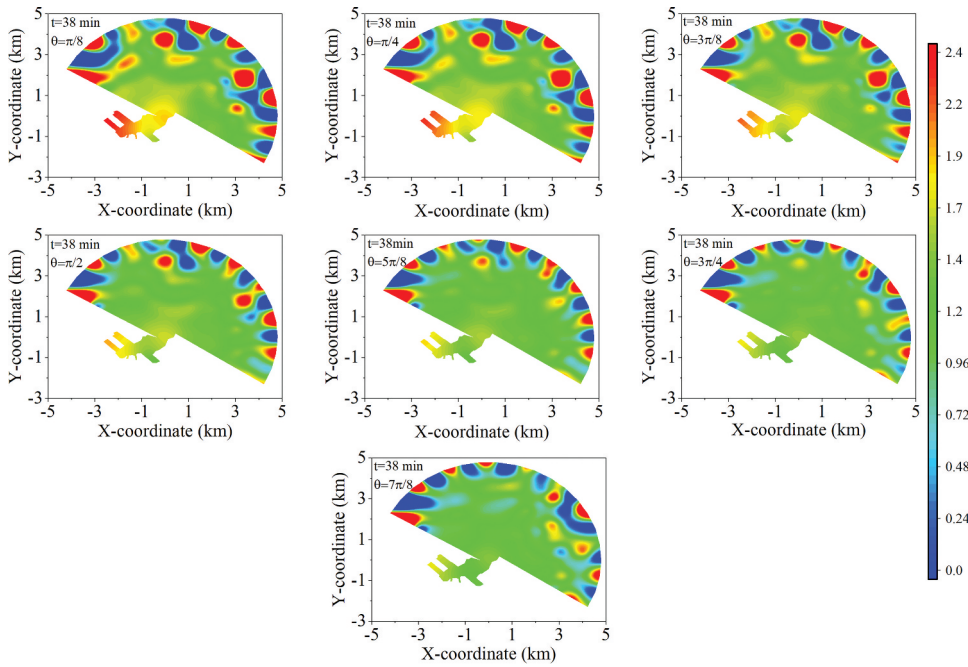


Figure 11. Wave height contour plots corresponding to third peak period (i.e., $t_3 = 38$ min) for the directional incident wave angle with from $\pi/8$ to $7\pi/8$.

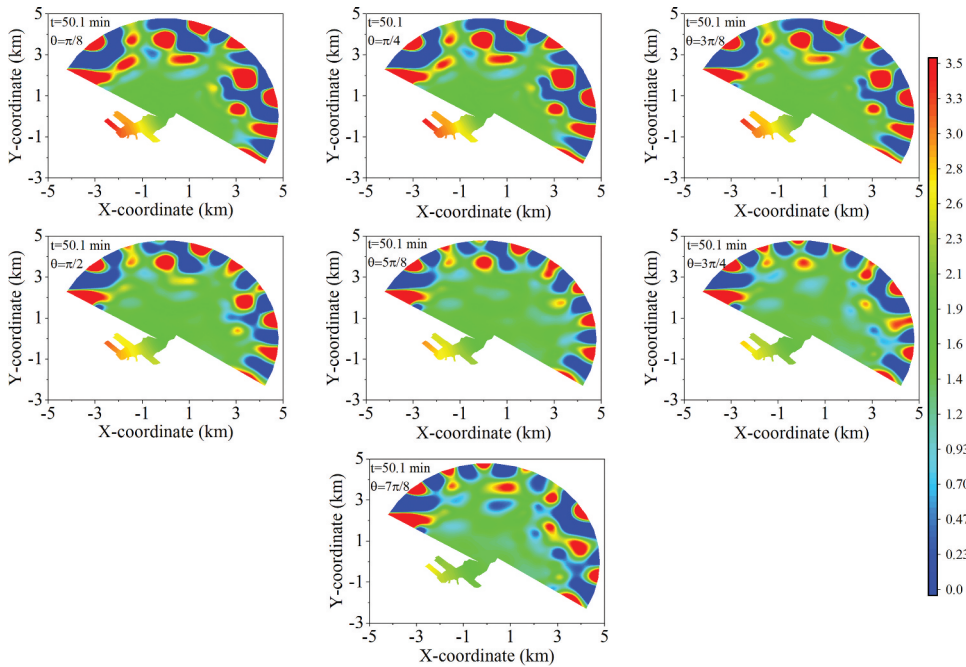


Figure 12. Wave height contour plots corresponding to the fourth peak period (i.e., $t_4 = 50.1$ min) for the directional incident wave angle with from $\pi/8$ to $7\pi/8$.

The strong wave elevation is obtained for the peak wave period at $t_4 = 50.1$ min in the interior of Paradip port range approximately from 1.6 m to 3.2 m. The location W3 is the most sensitive location inside the Paradip port for the wave period $t_4 = 50.1$ min at incident wave angles $\beta = \pi/8$ and $\pi/4$ (Figure 12). Overall, the wave elevation is consistent for different directional incident waves from angles $\beta = \pi/8$ and $7\pi/8$. Overall, the key location W1 and W4 is proposed as the safer locations inside the Paradip port for all directional incident waves. The incident waves with less peak wave period $t_1 = 7.6$ min produce lesser amplification as compared to high wave periods. Thus, both directions of the incident wave and peak wave period play an important role to estimate the wave height inside the Paradip port.

5. Discussion and Conclusion

In this study, a mathematical model based on BE with variable water depth is developed to examine the response of transient of long-wave inside the realistic port such as Paradip port, India under resonant conditions. The numerical solution of BE is obtained by using FEM with irregular mesh elements. The numerical accuracy is enhanced by utilizing the triangular non-uniform FEM mesh discretization. The present numerical scheme is validated with the previous studies of Lee (1971) [28] and Ippen and Goda (1963) [29], and Lepelletier (1981) [7] at the back wall of the fully open rectangular domain. The

convergence analysis of the present numerical scheme is also carried out through error analysis by utilizing the least square method and the result reveals that the present numerical model has a higher-order convergence (1.74) compared to BEM (1.56).

The surface wave elevation (η) is computed at the selected four key locations labelled as W1 to W4 inside the Paradip port for different incident wave angles ($\pi/8$ to $7\pi/8$). The peak wave periods are obtained at the period $t_1 = 7.6$ min, $t_2 = 19.6$ min, $t_3 = 38$ min, $t_4 = 50.1$ min, $t_5 = 67.8$ min, and $t_6 = 80.8$ min, respectively, in Paradip port. The wave amplitude is stronger for the incident wave with angles $\beta = \pi/8$ and $\pi/4$ as compared to other incident wave angles for all peak wave periods. In addition, W1 and W4 locations are the safest location in the Paradip port for the different peak wave periods and incident wave angles and W3 is the most sensitive location inside the port for all directional incident waves. The peak wave period (7.6 min) generates less amplification as compared to the high peak wave periods (19.6 min, 38 min, 50.1 min). The angular variation of the incident wave plays a crucial role to enhance/reduce the amplification inside the port. Overall, to prevent the damage of coastal structures and moored ship inside the Paradip port, the safe location with different wave periods and wave angles are identified to improve the resonance.

Acknowledgments

We would like to thank the Department of Applied Sciences (Mathematics), National Institute of Technology Delhi, India, and the financial grant received under SERB-DST (project file no: ECR/2016/001680), Government of India. The authors would like to acknowledge the reviewer's sincere suggestions and comments to improve our manuscript.

Funding

This work was supported by the Science and Engineering Research Board [ECR/2016/001680].

ORCID

Prashant Kumar  <http://orcid.org/0000-0001-8480-7490>

References

- [1] A.T. Ippen and Y. Goda, *Waves Induced Oscillation in Harbors: The Solution for a Rectangular Harbor Connected to the Open Sea*, Tech. Rep. 59 (1963). Massachusetts Institute of Technology Cambridge Hydrodynamics laboratory, Cambridge, pp. 282.
- [2] J.J. Lee, *Wave-induced oscillations in harbours of arbitrary geometry*, *J, Fluid Mech* 45 (1971), pp. 375–394.
- [3] P. Kumar, H. Zhang, and K.I. Kim, *Spectral density analysis for wave characteristics in Pohang New harbor*, *Pure Appl. Geophys* 171 (7) (2014), pp. 1169–1185. doi:10.1007/s00024-013-0710-x.
- [4] T.K. Tsay, W. Zhu, and P.L.F. Liu, *A finite element model for wave refraction, diffraction, reflection and dissipation*, *Appl. Ocean Res* 11 (1) (1989), pp. 33–38. doi:10.1016/0141-1187(89)90005-9.
- [5] Z. Demirbilek and V. Panchang, *CGWAVE: A coastal surface water wave model of the mild slope equation*, Tech. Rep. TR-CHL-98-26. Army Engineer Waterways Experiment Station Vicksburg MS. (1998)

- [6] T.H. Jung, S. Son, and Y. Ryu, *Finite element solution of linear waves on a sloping bottom boundary*, J. Coast. Res. 33 (2016), pp. 731–737.
- [7] T.G. Lepelletier, *Tsunamis - Harbor Oscillations Induced by Nonlinear Transient Long Waves*, Ph.D. diss., California Institute of Technology, 1981.
- [8] S.-B. Woo and P.L.-F. Liu, *Finite-element model for modified Boussinesq equations. II: Applications to nonlinear harbor oscillations*, Journal of Waterway, Port, Coastal, and Ocean Engineering 130 (1) (2004), pp. 17–28. doi:10.1061/(ASCE)0733-950X(2004)130:1(17).
- [9] J. Gao, C. Ji, O. Gaidai, Y. Liu, and X. Ma, *Numerical investigation of transient harbor oscillations induced by N-waves*, Coastal Engineering 125 (2017), pp. 119–131. doi:10.1016/j.coastaleng.2017.03.004.
- [10] D.H. Peregrine, *Long Waves on a Beach*, J. Fluid Mech 27 (4) (1967), pp. 815–827. doi:10.1017/S0022112067002605.
- [11] P.A. Madsen and O.R. Sorensen, *A new form of the Boussinesq equations with improved linear dispersion characteristics. Part 2. A Slowly-varying Bathymetry*, Coastal Engineering 18 (3–4) (1992), pp. 183–204. doi:10.1016/0378-3839(92)90019-Q.
- [12] G. Wei and J.T. Kirby, *Time-dependent numerical code for extended Boussinesq equations*, Journal of Waterway, Port, Coastal, and Ocean Engineering 121 (5) (1995), pp. 251–261. doi:10.1061/(ASCE)0733-950X(1995)121:5(251).
- [13] D. Ambrosi and L. Quartapelle, *A Taylor–Galerkin Method for Simulating Nonlinear Dispersive Water Waves*, J. Comput. Phys. 146 (2) (1998), pp. 546–569. doi:10.1006/jcph.1998.6027.
- [14] J.S. Antunes do Carmo, F.J. Seabra Santos, and E. Barthelemy, *Surface waves propagation in shallow water: A finite element model*, Internat. J. Numer. Methods Fluids 16 (6) (1993), pp. 447–459. doi:10.1002/flid.1650160602.
- [15] Y.S. Li, S.X. Liu, Y.X. Yu, and G.Z. Lai, *Numerical modeling of Boussinesq equations by finite element method*, Coastal Engineering 37 (2) (1999), pp. 97–122. doi:10.1016/S0378-3839(99)00014-9.
- [16] O.R. Sorensen, H.A. Schäffer, and L.S. Sørensen, *Boussinesq-type modelling using an unstructured finite element technique*, Coastal Engineering 50 (4) (2004), pp. 181–198. doi:10.1016/j.coastaleng.2003.10.005.
- [17] S.B. Woo and P.L.F. Liu, *Finite-element model for modified Boussinesq equations. I: Model development*, Journal of Waterway, Port, Coastal, and Ocean Engineering 130 (1) (2004), pp. 1–16. doi:10.1061/(ASCE)0733-950X(2004)130:1(1).
- [18] S.-B. Woo and L.-F. Liu, *A Petrov-Galerkin finite element model for one-dimensional fully non-linear and weakly dispersive wave propagation*, International Journal for Numerical Methods in Fluids 37 (5) (2001), pp. 541–575. doi:10.1002/flid.186.
- [19] T.Y. Wu, *Tsunamis. Proc. National Science Foundation Workshop*, Tetra Tech. Inc, Pasadena, 1979, pp. 110–149.
- [20] P. Kumar, H. Zhang, D.A. Yuen, and K.I. Kim, *Wave field analysis in a harbor with irregular geometry through boundary integral of Helmholtz equation with corner contributions*, Comput Fluids, 88 (2013), pp. 287–297. doi:10.1016/j.compfluid.2013.09.020
- [21] P. Kumar and Gulshan, *Extreme wave-induced oscillation in Paradip port under the resonance conditions*, Pure and Applied Geophysics 174 (12) (2017), pp. 4501–4517. doi:10.1007/s00024-017-1646-3.
- [22] P. Kumar and Gulshan, *Theoretical analysis of extreme wave oscillation in Paradip Port using a 3-D boundary element method*, Ocean Engineering 164 (2018), pp. 13–22. doi:10.1016/j.oceaneng.2018.06.029.
- [23] R.P. Kumar and Rajni, *Spectral boundary element modeling of water waves in Pohang New Harbor and Paradip Port*, Ocean Engineering. 196 (2019), pp. 106765 (Art. Nr).
- [24] M. Guerrini, G. Bellotti, Y. Fan, and L. Franco, *Numerical modelling of long waves amplification at Marina di Carrara Harbour*, Appl. Ocean Res. 48 (2014), pp. 322–330. doi:10.1016/j.apor.2014.10.002.
- [25] P. Kumar and Rupali, *Modeling of shallow water waves with variable bathymetry in an irregular domain by using Hybrid Finite Element Method*, Ocean Engineering 165 (2018), pp. 386–398. doi:10.1016/j.oceaneng.2018.07.024.

- [26] D. Schmicker, S. Duczec, S. Liefold, and U. Gabbert, *Wave propagation analysis using high-order finite element methods: Spurious oscillations excited by internal element eigen frequencies*, *Technische Mechanik* 34 (2014), pp. 51–71.
- [27] T.G. Lepelletier and F. Raichlen, *Harbor Oscillations Induced by Nonlinear Transient Long Waves*, *Journal of Waterway, Port, Coastal, and Ocean Engineering* 113 (4) (1987), pp. 381–400. doi:10.1061/(ASCE)0733-950X(1987)113:4(381).
- [28] J.J. Lee, *Wave-induced oscillations in harbours of arbitrary geometry*, *J. Fluid Mech.* 45 (1971), pp. 375–394.
- [29] A. T. Ippen and Y. Goda, *Waves induced oscillation in harbors: the solution for a rectangular harbor connected to the open sea*, Tech. Rep. 59, Massachusetts Institute of Technology Cambridge Hydrodynamics laboratory, Cambridge, 1963. p. 282.
- [30] T.J.R. Hughes, K.S. Pister, and R.L. Taylor, *Implicit-explicit finite elements in nonlinear transient analysis*, *Comput. Methods Appl. Mech. Eng.* 17-18 (1979), pp. 159–182. doi:10.1016/0045-7825(79)90086-0.
- [31] P. Kumar, S. Kaur, E. Weller, and S.K. Min, *Influence of Natural Climate Variability on the Extreme Ocean Surface Wave Heights Over the Indian Ocean*, *J. Geophys. Res. Ocean.* 124 (8) (2019), pp. 6176–6199. doi:10.1029/2019JC015391.